Progress In Electromagnetics Research, Vol. 160, 19–27, 2017

Broadband Generation of Orbital Angular Momentum Carrying Beams in RF Regimes

Fuchun Mao[1], Ming Huang[1, *], Tinghua Li[2], Jialin Zhang[3], and Chengfu Yang[1]

Abstract—We propose a novel approach for the broadband generation of orbital angular momentum (OAM) carrying beams based on the Archimedean spiral. The mechanism behind the antenna is theoretically analyzed and further validated by numerical simulation and physical measurement. The results show that the spiral-based antenna is able to reliably generate the OAM carrying beams in an ultra-wide frequency band. Of particular interest is the fact that the mode number of radiated beams is reconfigurable with a change in operating frequency. Prototypes of a single-arm spiral antenna (SASA), a multi-arm spiral antenna (MASA), and a compact multi-arm spiral antenna (CMASA) are investigated and demonstrated to support our arguments. The proposed approach provides an effective and competitive way to generate OAM carrying beams in radio and microwave bands, which may have potential in wireless communication applications due to its characteristics of simplicity, broadband capacity and reconfiguration opportunities.

1. INTRODUCTION

In recent years, electromagnetic fields carrying orbital angular momentum (OAM) have captured attention due to their fascinating properties and broad application prospects in various fields such as quantum entanglement [1], electron vortex [2, 3], microscopy and imaging [4, 5], neutron control [6], remote sensing [7], and optical tweezers [8]. Especially in information science [9–12], the mutually orthogonal feature of OAM modes may increase spectral efficiency and system capacity. Understanding how to generate OAM beams flexibly and simply is an essential issue. Compared to optical OAM generators [13–20], radio frequency (RF) OAM generators are still in the initial research stage.

To the best of our knowledge, five OAM generators in the RF band have been reported, including a circular phased antenna array [21, 22], a helical paraboloid antenna [23], a circular polarized patch [24], a circular loop antenna [25], and an electromagnetic metasurface [26]. Unfortunately, all of these OAM generators have some defects more or less. In more concrete terms, the phased antenna array performs well in the reconfiguration mode, but it needs a complex feed network, which is hard to implement [27]. The helical paraboloid antenna has a bulky structure and no ability for mode reconfiguration. The circular polarized patch and the circular loop antenna only work in a very narrow frequency band because of their resonant properties [28, 29]. The metasurface is not suitable for the miniaturized scenario, as it requires a large geometry with respect to the operating wavelength [30]. Therefore, it is necessary to explore an alternative approach to generate OAM carrying beams that overcomes these defects.

In this paper, we propose a method for broadband generation of the OAM carrying beams based on the Archimedean spiral. Theoretical analysis is conducted to explain the work principle of the new

Received 23 August 2017, Accepted 7 October 2017, Scheduled 25 October 2017
* Corresponding author: Ming Huang (huangming@ynu.edu.cn).
[1] Wireless Innovation Lab of Yunnan University, School of Information Science and Engineering, Kunming, Yunnan 650091, China. [2] The Technical Center of China Tobacco Yunnan Industrial Co. Ltd., Kunming, Yunnan 650231, China. [3] Radio Monitoring Center of Yunnan Province, Kunming, Yunnan 650228, China.

OAM generation approach. Then, simulation models of a single-arm spiral antenna (SASA), a multi-arm spiral antenna (MASA), and a compact multi-arm spiral antenna (CMASA) are performed to verify the theoretical results. Further, an experimental prototype of the MASA is fabricated and measured. Compared with existing OAM generators in the RF regime, the proposed spiral-based OAM antenna performs better in terms of bandwidth, mode reconfiguration, and structural complexity. Therefore, it may be suitable for broad applications in the field of OAM-based wireless communication systems.

2. MODEL OF THE ANTENNA

The polar coordinate equation of the Archimedean curve is expressed as $\rho = \rho_0 + \delta(\varphi - \varphi_0)$, where ρ, ρ_0, δ, φ_0 and φ are the radial distance, initial radial distance, spiral constant, initial angle and winding angle, respectively. This structure can be used to design SASA. As is well known, SASA supports a circular active region when excited by a current travelling wave, which is shown in Fig. 1(a), in which the shaded annular area represents the active region. Radiation from the spiral comes mainly from an equivalent travelling ring of current with the circumference $l\lambda_g$ in the active region [31–33]. l and λ_g are, respectively, the integer and waveguide wavelength. For the convenience of theoretical analysis, the travelling ring of the current is mathematically modeled as a circular-ring quasi array with tangentially placed elements, as depicted in Fig. 1(b), where $P(\theta, \varphi, r)$ is an observation point located in the far-field zone. The array factor of the quasi array is found as:

$$S(\theta, \varphi) = \frac{1}{N} \sum_{n=1}^{N} e^{j[ka \sin\theta \cos(\varphi - \varphi_n) + l\varphi_n]}, \tag{1}$$

where N, φ_n, a, and k are, respectively, the number of elements, azimuthal angle of the nth element, radius of the array, and the wave number. Using the integral form of the Bessel function and the limitation $N \to \infty$, the normalized radiation vector $\vec{F}(\theta, \varphi, z)$ of the array can be deduced as:

$$F_\theta = \frac{l}{z} e^{jl(\varphi + \pi/2)} \cos\theta J_l(z), \quad F_\varphi = j e^{jl(\varphi + \pi/2)} J_l'(z) \tag{2}$$

where $z = ka \sin\theta$, and $J_l(\cdot)$ and $J_l'(\cdot)$ are the Bessel function of the first kind and its derivative, respectively. The corresponding electric field component of the radiated beam is obtained by $\vec{E} = (jkI_0\eta/2)e^{jkr}\vec{F}$, and the magnetic field component by $\vec{H} = \vec{r} \times \vec{E}/r\eta$, where η stands for the intrinsic impedance of free space, and I_0 is the current magnitude of the elements. Thus the electric field, for instance, can be deduced as

$$E_\theta = e^{jl(\varphi + \pi/2)} e^{-jkr} \frac{l}{z} \frac{jk60\pi a}{r} \cos\theta J_l(z) \tag{3a}$$

$$E_\varphi = j e^{jl(\varphi + \pi/2)} e^{-jkr} \frac{jk60\pi a}{r} J_l'(z) \tag{3b}$$

$$E_r = e^{jl(\varphi + \pi/2)} \left[\frac{l}{z} J_l(z) \cos\varphi - j J_l'(z) \sin\varphi \right] \frac{jk60\pi a}{r} \frac{1}{\cos\theta \sin\varphi} e^{-jkr}. \tag{3c}$$

Based on the above analysis, one can find that the radiated fields are mainly characterized by the Bessel functions ($J_l(\cdot)$ and $J_l'(\cdot)$) and the phase factor $e^{jl(\varphi + \pi/2)}$. Bessel functions transform the generated waves into hollow beams, which, with toroidal-shape intensity distribution in its transverse field, is one of the classical features of OAM carrying beams. Furthermore, the most essential characteristic of an OAM carrying beam is the spiral phase structure, which here is controlled and ensured by the phase factor $e^{jl(\varphi + \pi/2)}$. The mode number of the radiated OAM carrying beam is exactly equal to l. The numerical results based on these formulas are shown in Fig. 2, which depicts the typical behavior noted above of OAM carrying beams.

The radius of the active region, namely $a = l\lambda_g/2\pi$, is synchronous varying with the operating frequency. Thus, the spiral can generate OAM carrying beams in an ultra-wide frequency band. This broadband property can also be explained by the spiral's input impedance. The input impedance of a spiral embedded in a dielectric substrate with relative permittivity ε_r is defined as $Z_{in} = 0.5\sqrt{\mu_0/\varepsilon_0\varepsilon_r}$,

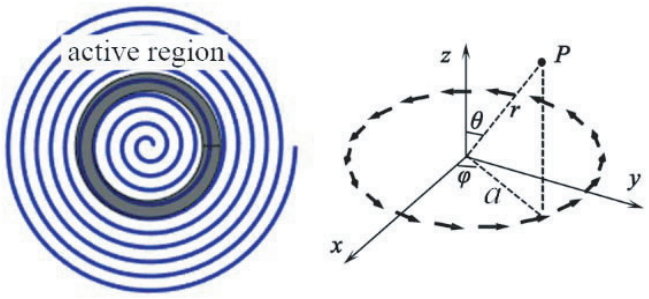

(a) (b)

Figure 1. Schematic diagram and equivalent mathematical model. (a) The SASA excited by a current travelling wave. (b) The equivalent model of the active region.

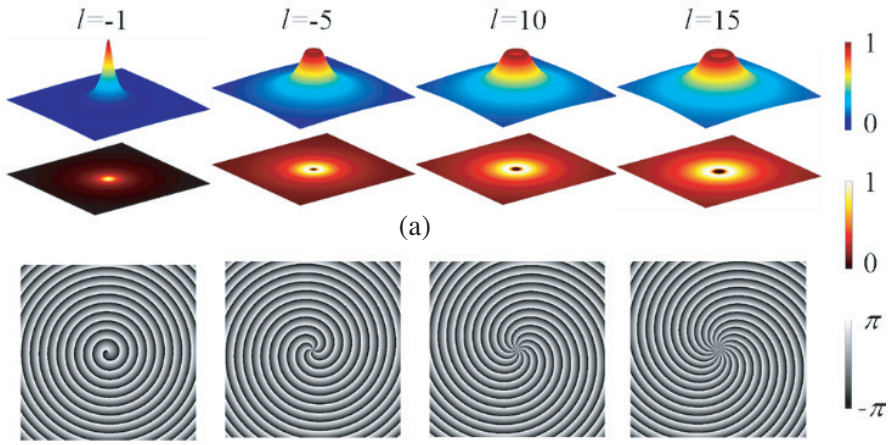

(a)

(b)

Figure 2. Calculated intensity and phase patterns of E_φ based on the theoretical formulas. (a) The normalized three dimensional (3D) and two dimensional (2D) intensity distribution. (b) Phase distribution.

which shows frequency-independent behavior. The reason for this is that the spiral structure is self-complementary.

This analysis has not been carried out to the point of a rigorous analytic solution for radiated fields generated by the spiral. However, this explanation for the radiating mechanism of the SASA is in accord with the following observations, and is helpful for designing new spiral-based OAM generators. The methodology of the active region is adopted, based on the fact that the radiation from the actual spiral current is approximated to the radiation from an equivalent travelling ring of current.

3. CALCULATIONS AND DISCUSSIONS

3.1. Single-Arm Spiral Antenna Strategy

The configuration of the proposed SASA is depicted in Fig. 3, in which r_s=50 mm and h_s=1 mm are, respectively, the radius and thickness of the substrate; r_g=12 mm is the radius of the ground; w_s=2 mm denotes the width of spacing; and w_m= 2 mm stands for the width of the spiral arm. The proposed SASA is composed by the metal spiral arm, a small ground, a dielectric substrate, and the SMA connector. The dielectric substrate is chosen as FR4 with a relative permittivity of ε_r = 4.4. The radius of the ground is much smaller than substrate to avoid the resonance that may occur at the spiral arm and prevent the radiation of OAM.The antenna is performed by the commercial electromagnetic analysis software HFSS. The behavior of the wave front and intensity for the radiated field are investigated using the full-wave simulation method.

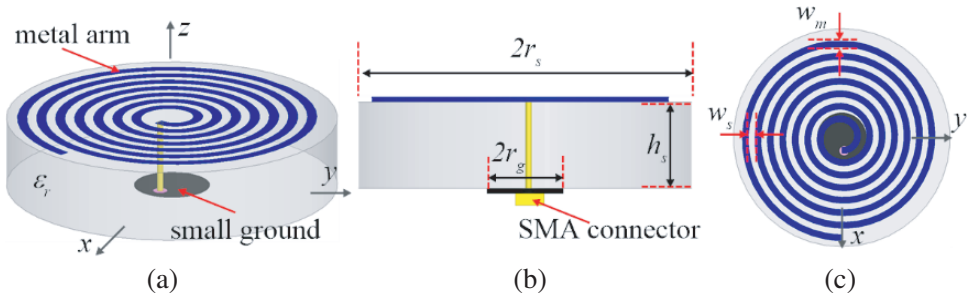

Figure 3. Geometric design of the proposed SASA. (a) Perspective view. (b) Cross-section view. (c) Top view.

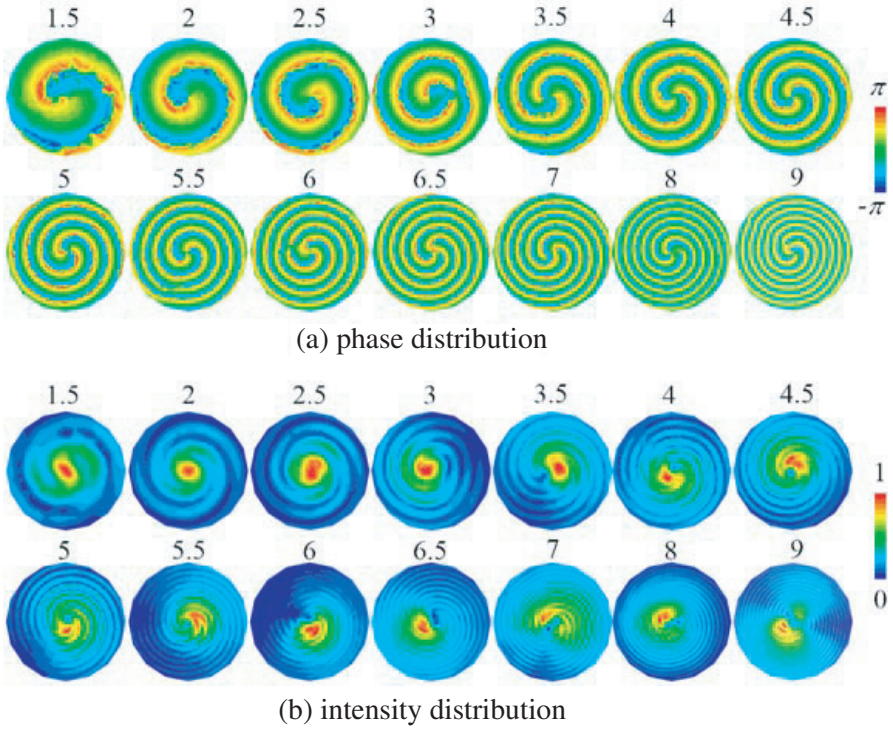

Figure 4. Numerical results of SASA. (a) The phase distribution within an identical observation window. (b) The intensity distribution of electric field within the same observation window that used by (a).

The simulated results of phase and intensity of the radiated fields are shown in Fig. 4, in which the superscript digit represents the working frequency. One may easily see from the phase distributions of electric field that the presented SASA successfully radiates the OAM carrying beams as expected (Fig. 4(a)). Note that the mode number of the radiated OAM carrying beams varies from 1 to 3, with the operating frequency increasing from 1.5 GHz to 9 GHz. More precisely, according to our calculations, the mode number of the radiated beam equals 1 in the band of [1.3, 3.25] GHz, 2 in [3.45, 6.1] GHz, and 3 in [6.25, 10.5] GHz. In other words, the SASA works in the modes of $1\cdot\lambda_g$, $2\cdot\lambda_g$, and $3\cdot\lambda_g$, i.e., l=1, 2, 3, in these three bands, respectively. Compared to reported resonant OAM generators, the bandwidth of the SASA is quite wide. The results also reveal another merit of SASA: reconfigurability of the OAM state without any geometric changes. The corresponding normalized intensity distributions are drawn in Fig. 4(b), from which one can determine the vortex movement of the radiated fields. In addition, a weak field region appears near the center of the beams and increases its own size as l increases.

3.2. Multi-Arm Spiral Antenna Strategy

In order to expand the design methods of the spiral-base OAM antenna, we arrange multiple spirals into a circular ring array to form the MASA, which is drawn in Figs. 5(a)–(b). Note that the spirals are independently fed by identical signals in this configuration, in order to make each spiral radiate an OAM carrying field with a mode number l at the same frequency. The superpositions and interferences among these fields will eventually form a new OAM carrying field with a mode number of $L{=}n \cdot l$, where n is the number of spirals. This intuitive inference is validated by the simulation results portrayed in Figs. 5(c)–(h). For simplicity and without a loss of generality, we choose $n{=}\,2$ as the example in this instance. The behavior of the radiated field at 2 GHz and 8 GHz are depicted in Figs. 5(c)–(e), and Figs. 5(f)–(h), respectively. Each arm of the 2-arm spiral antenna operates in state $l = 1$ and $l = 2$, corresponding to 2 GHz and 8 GHz. Accordingly, the 2-arm spiral antenna produces the OAM carrying beam with a mode number of $L{=}\,2 \cdot 1$ for 2 GHz, and $L{=}\,2 \cdot 2$ for 8 GHz. In short, not only the correctness of $L{=}n \cdot l$, but also the reconfigurability of the OAM state, is verified.

As mentioned above, another merit of the spiral antenna is the broadband characteristic. Here, the word "broadband" has two meanings: the antenna radiates OAM carrying beams over broadband, and

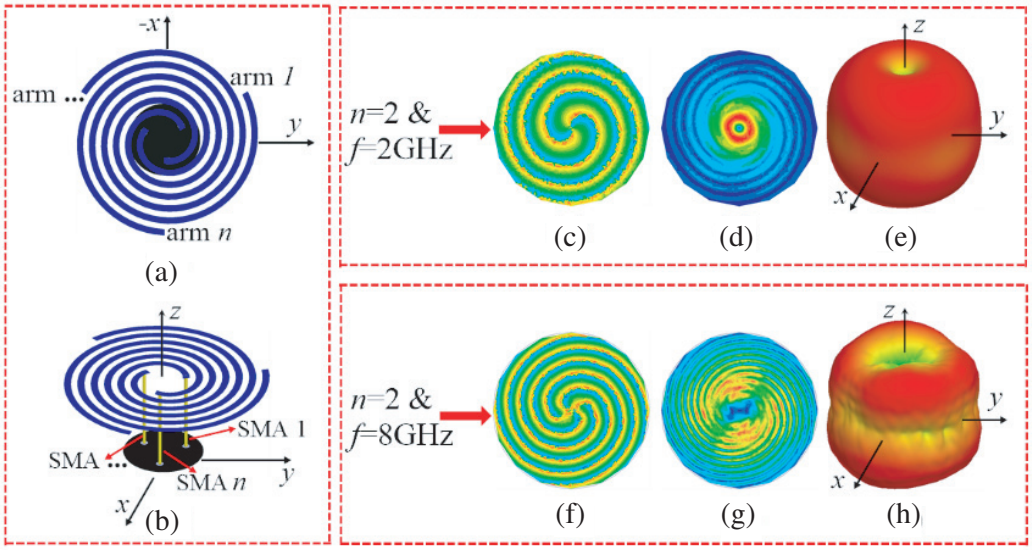

Figure 5. Geometric design and simulated results of the MASA. (a)–(b) Schematic of the MASA. For $n = 2$, $f = 2$ GHz, (c) phase, (d) intensity, (e) 3D polar radiation. For $n = 2$, $f = 8$ GHz, (f) phase, (g) intensity, (h) 3D polar radiation.

Figure 6. Photos of the 2-arm spiral antenna. (a) Top view. (b) Bottom view.

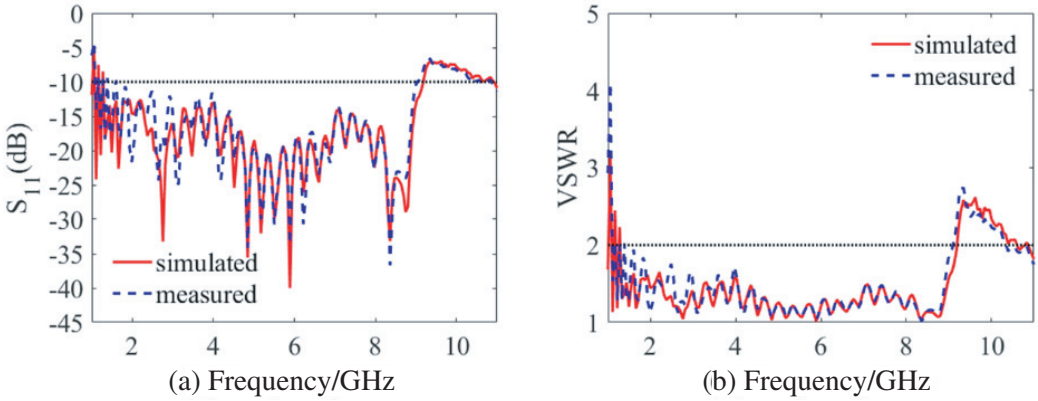

Figure 7. Comparison of the simulation and experiment. (a) S_{11}. (b) VSWR.

the antenna has an impedance match over a wide band. The first point is supported by Fig. 4. However, to verify the second point, we further fabricated and measured the 2-arm spiral antenna. The relevant photos are illustrated in Fig. 6. The cylindrical back cavity (BC) and a 2-way power splitter are used for a good uni-directional radiation in the experiment. The excitation is first connected to the input of the splitter, and then two signals with equal amplitude and phase are received at the outputs and fed to different spirals. The voltage standing-wave ratio (VSWR) and return loss (S_{11}) of the fabricated antenna are measured by a vector network analyzer (Agilent Technologies E8362B 10 MHz $\sim$ 20 GHz) through a flexible test port cable (Agilent 87131F). The corresponding results are shown in Fig. 7, where the measurements are in good agreement with the simulations. The slight discrepancies appearing at some frequencies result from fabrication error, dielectric loss, insertion loss, and measuring error and so on.One may see that the 2-arm spiral antenna achieves a good impedance match over the frequency range [1.16, 9.13] GHz with $S_{11} < -10$ dB and VSWR < 2. This performance of bandwidth is far better than that of other reported OAM generators based on the resonance principle [23–25, 27–29].

3.3. Compact Multi-Arm Spiral Antenna Strategy

Due to the need for a special power-splitting feeding network, the MASA is complicated and bulky. However, when w_m is small enough, we can reduce the initial radial distance as $\rho_0 = 0$ mm and directly connect the n spirals. This will greatly simplify the geometry of the MASA and make it more compact, namely CMASA. As depicted in Fig. 8, all the spiral arms are connected to a small junction with diameter $d = 2w_m$, and the n SMA connectors depicted in Fig. 5(b) are replaced with a single one. This practice is feasible because the impedance of the n branches is equal, which means that the excitation currents flowing from the junction to the end of the spiral arms, i.e., $I_0, I_1, \ldots, I_n$, are very close, both in amplitude and phase, when the size of the junction is small. In other words, the function of an n-way

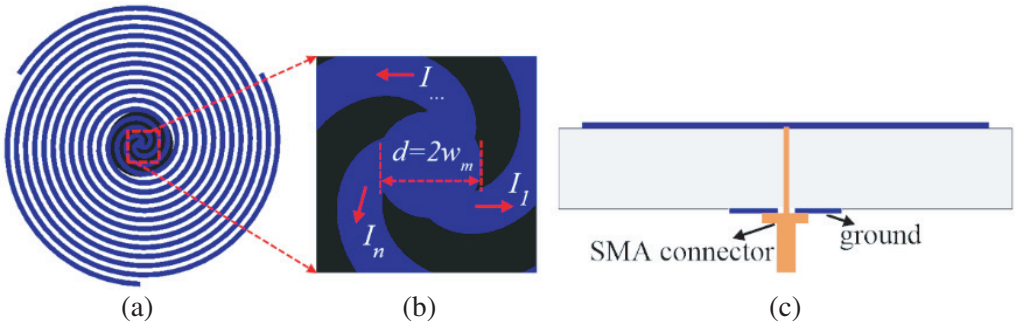

Figure 8. The schematic of the CMASA. (a) Top view. (b) A zoomed-in view of the center of (a). (c) The cross section.

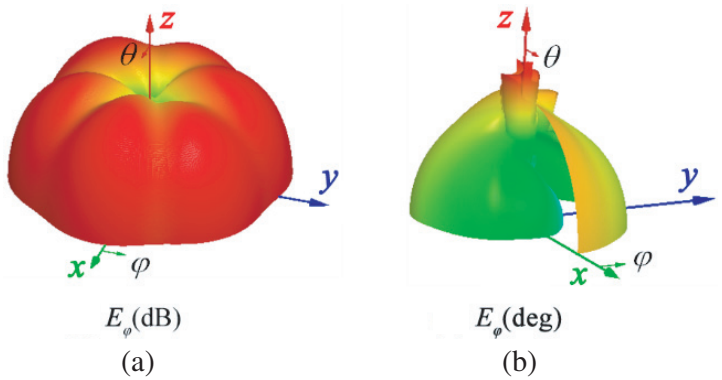

Figure 9. Simulated 3D radiation and phase pattern of a 3-arm spiral antenna at 2 GHz. (a) Amplitude. (b) Cumulative phase.

power splitter is inherently realized by the simplified configuration.

Taking $n = 3$ as the example, the simulated radiation and phase patterns of E_φ are shown in Fig. 9. The 3D polar radiation pattern (Fig. 9(a)) reveals a central hole that is characteristic of OAM carrying beams. The spiral form of the phase pattern, plotted in polar coordinates (Fig. 9(b)), corresponds to the linear variation of the phase versus the roll angle φ. Both the amplitude and phase show an OAM carrying beam with $l = 3$.

4. CONCLUSIONS

An approach based on the Archimedean spiral is proposed to generate OAM carrying beams in the RF regime. The results of theoretical analysis, numerical simulation, and actual measurement prove the feasibility, validity and superiority of the presented method. Multiple prototypes of SASA, MASA, and CMASA are described for a complete investigation that is significant for the design of the spiral-based OAM antenna in the RF band. The proposed spiral-based OAM antenna represents a major advance in design with respect to previously reported OAM generators in terms of bandwidth, mode reconfiguration, and structural complexity, and as such it has considerable potential for many kinds of OAM-based wireless applications.

ACKNOWLEDGMENT

This work was supported by the National Natural Science Foundation of China (Grant Nos. 61461052), the Specialized Research Fund for the Doctoral Program of Higher Education (Grant No. 20135301110003), the Seventh of Yunnan University Graduate Student Scientific Research Project (Grant No. ynuy201443), and the doctoral award for the academic newcomers (2014) of Yunnan Province.

REFERENCES

1. Krenn, M., M. Malik, M. Erhard, and A. Zeilinger, "Orbital angular momentum of photons and the entanglement of Laguerre-Gaussian modes," *Phil. Trans. R. Soc. A*, Vol. 375, 20150442, 2017.
2. McMorran, B. J., A. Agrawal, P. A. Ercius, V. Grillo, A. A. Herzing, T. R. Harvey, M. Linck, and J. S. Pierce, "Origins and demonstrations of electrons with orbital angular momentum," *Phil. Trans. R. Soc. A*, Vol. 375, 20150434, 2017.
3. Shiloh, R., Y. Tsur, R. Remez, Y. Lereah, B. A. Malomed, V. Shvedov, C. Hnatovsky, W. Krolikowski, and A. Arie, "Unveiling the orbital angular momentum and acceleration of electron beams," *Phys. Rev. Lett.*, Vol. 114, No. 9, 096102, 2015.

4. Ritsch-Marte, M., "Orbital angular momentum light in microscopy," *Phil. Trans. R. Soc. A*, Vol. 375, 20150437, 2017.
5. Fischer, P., "X-ray imaging of magnetic structures," *IEEE Transactions on Magnetics*, Vol. 51, No. 2, 1–31, 2015.
6. Clark, C. W., R. Barankov, M. G. Huber, M. Arif, D. G. Cory, and D. A. Pushin, "Controlling neutron orbital angular momentum," *Nature*, Vol. 525, No. 7570, 504–506, 2015.
7. Uribe-Patarroyo, N., A. Fraine, D. S. Simon, O. Minaeva, and A. V. Sergienko, "Object identification using correlated orbital angular momentum states," *Phys. Rev. Lett.*, Vol. 110, No. 4, 043601, 2013.
8. Padgett, M. and R. Bowman, "Tweezers with a twist," *Nat. Photonics*, Vol. 5, No. 6, 343–348, 2011.
9. Yuan, Y., T. Lei, Z. Li, Y. Li, S. Gao, Z. Xie, and X. Yuan, "Beam wander relieved orbital angular momentum communication in turbulent atmosphere using Bessel beams," *Scientific Reports*, Vol. 7, 2017.
10. Ren, Y., L. Li, G. Xie, Y. Yan, Y. Cao, H. Huang, N. Ahmed, Z. Zhao, P. Liao, C. Zhang, G. Caire, A. F. Molisch, M. Tur, and A. E. Willner, "Line-of-sight millimeter-wave communications using orbital angular momentum multiplexing combined with conventional spatial multiplexing," *IEEE Transactions on Wireless Communications*, 2017.
11. Yu, S., "Potentials and challenges of using orbital angular momentum communications in optical interconnects," *Optics Express*, Vol. 23, No. 3, 3075–3087, 2015.
12. Bozinovic, N., Y. Yue, Y. Ren, M. Tur, P. Kristensen, H. Huang, A. E. Willner, and S. Ramachandran, "Terabit-scale orbital angular momentum mode division multiplexing in fibers," *Science*, Vol. 340, No. 6140, 1545–1548, 2013.
13. Devlin, R. C., A. Ambrosio, D. Wintz, S. L. Oscurato, A. Y. Zhu, M. Khorasaninejad, J. Oh, P. Maddalena, and F. Capasso, "Spin-to-orbital angular momentum conversion in dielectric metasurfaces," *Optics Express*, Vol. 25, No. 1, 377–393, 2017.
14. Cai, X., J. Wang, M. J. Strain, B. Johnson-Morris, J. Zhu, M. Sorel, J. L. O'Brien, M. G. Thompson, and S. Yu, "Integrated compact optical vortex beam emitters," *Science*, Vol. 338, No. 6105, 363–366, 2012.
15. Zhang, C., L. Deng, W. J. Hong, W. X. Jiang, J. F. Zhu, M. Zhou, L. Wang, S. F. Li, and B. Peng, "Three-dimensional simultaneous arbitrary-way orbital angular momentum generator based on transformation optics," *Scientific Reports*, Vol. 6, 2016.
16. Lei, T., M. Zhang, Y. Li, P. Jia, G. N. Liu, X. Xu, Li Z., C. Min, J. Lin, C. Yu, H. Niu, and X. Yuan, "Massive individual orbital angular momentum channels for multiplexing enabled by Dammann gratings," *Light: Science & Applications*, Vol. 4, e257, 2015.
17. Li, S. and Z. Wang, "Generation of optical vortex based on computer-generated holographic gratings by photolithography," *Appl. Phys. Lett.*, Vol. 103, No. 14, 141110, 2013.
18. Dall, R., M. D. Fraser, A. S. Desyatnikov, G. Li, S. Brodbeck, M. Kamp, C. Schneider, S. Höfling, and E. A. Ostrovskaya, "Creation of orbital angular momentum states with chiral polaritonic lenses," *Phys. Rev. Lett.*, Vol. 113, No. 20, 200404, 2014.
19. Niederriter, R. D., M. E. Siemens, and J. T. Gopinath, "Continuously tunable orbital angular momentum generation using a polarization-maintaining fiber," *Optics Letters*, Vol. 41, No. 14, 3213–3216, 2016.
20. Gambini, F., P. Velha, C. J. Oton, and S. Faralli, "Orbital angular momentum generation with ultra-compact bragg-assisted silicon microrings," *IEEE Photonics Technology Letters*, Vol. 28, No. 21, 2355–2358, 2016.
21. Thidé, B., H. Then, J. Sjöholm, K. Palmer, J. Bergman, T. D. Carozzi, Ya. N. Istomin, N. H. Ibragimov, and R. Khamitova, "Utilization of photon orbital angular momentum in the low-frequency radio domain," *Phys. Rev. Lett.*, Vol. 99, No. 8, 087701, 2007.
22. Mohammadi, S. M., L. K. Daldorff, J. E. Bergman, R. L. Karlsson, B. Thidé, K. Forozesh, T. D. Carozzi, and B. Isham, "Orbital angular momentum in radio — A system study," *IEEE Trans.*

Antennas Propag., Vol. 58, No. 2, 565–572, 2010.

23. Tamburini, F., E. Mari, A. Sponselli, B. Thidé, A. Bianchini, and F. Romanato, "Encoding many channels on the same frequency through radio vorticity: First experimental test," *New J. Phys.*, Vol. 14, No. 3, 033001, 2012.
24. Barbuto, M., F. Trotta, F. Bilotti, and A. Toscano, "Circular polarized patch antenna generating orbital angular momentum," *Progress In Electromagnetics Research*, Vol. 148, 23–30, 2014.
25. Zheng, S., X. Hui, X. Jin, H. Chi, and X. Zhang, "Transmission characteristics of a twisted radio wave based on circular traveling-wave antenna," *IEEE Trans. Antennas Propag.*, Vol. 63, No. 4, 1530–1536, 2015.
26. Yu, S., L. Li, G. Shi, C. Zhu, X. Zhou, and Y. Shi, "Design, fabrication, and measurement of reflective metasurface for orbital angular momentum vortex wave in radio frequency domain," *Appl. Phys. Lett.*, Vol. 108, No. 12, 121903, 2016.
27. Wei, W., K. Mahdjoubi, C. Brousseau, and O. Emile, "Generation of OAM waves with circular phase shifter and array of patch antennas," *Electronics Letters*, Vol. 51, No. 6, 442–443, 2015.
28. Chen, J. J., Q. N. Lu, F. F. Dong, J. J. Yang, and M. Huang, "Wireless OAM transmission system based on elliptical microstrip patch antenna," *Optics Express*, Vol. 24, No. 11, 11531–11538, 2016.
29. Hui, X., S. Zheng, Y. Chen, Y. Hu, X. Jin, H. Chi, and X. Zhang, "Multiplexed millimeter wave communication with dual orbital angular momentum (OAM) mode antennas," *Scientific Reports*, Vol. 5, 10148, 2015.
30. Yu, S., L. Li, G. Shi, C. Zhu, and Y. Shi, "Generating multiple orbital angular momentum vortex beams using a metasurface in radio frequency domain," *Appl. Phys. Lett.*, Vol. 108, No. 24, 241901, 2016.
31. Kaiser, J. A., "The Archimedean two-wire spiral antenna," *IRE Transactions on Antennas & Propagation*, Vol. 8, No. 3, 312–323, 1960.
32. Nakano, H., R. Satake, and J. Yamauchi, "Extremely low-profile, single-arm, wideband spiral antenna radiating a circularly polarized wave," *IEEE Trans. Antennas Propag.*, Vol. 58, No. 5, 1511–1520, 2010.
33. Mcfadden, M. and W. R. Scott, "Analysis of the equiangular spiral antenna on a dielectric substrate," *IEEE Trans. Antennas Propag.*, Vol. 55, No. 11, 3163–3171, 2007.